
Explaining Spectral Line Profiles in the Horsehead Nebula Using Cloud Surface Curvature

Student
Ducheng Lu

Supervisors
Franck Le Petit (LERMA)
Emeric Bron (LERMA)

Jan 2025

Contents

1	Introduction	2
1.1	Photodissociation Regions (PDRs)	2
1.2	The Horsehead Nebula	2
2	Data	4
3	Methods	4
3.1	The MeudonPDR code	4
3.1.1	Constant Pressure vs. Constant Density	5
3.1.2	Models with Exact Radiative Transfer of H ₂	6
3.1.3	Models with Surface Chemistry	7
3.2	Geometry	8
3.3	Column Density	8
3.4	Radiative transfer equation	9
3.5	Convolution	11
4	Results and Discussion	11
4.1	Cloud Surface Curvature	11
4.2	Line Profiles	11
5	Conclusions	11

Abstract

Context.

Aim.

Methods.

Results.

Abstract

Contexte.

Objectif.

Méthodes.

Résultats.

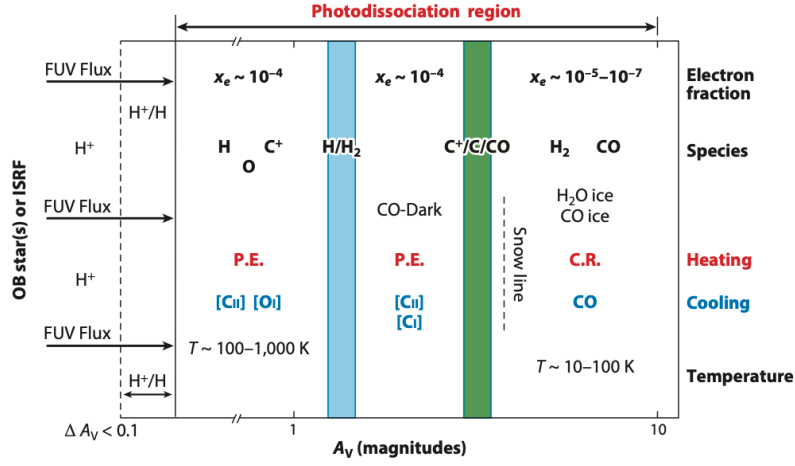


Figure 1: Schematic of a photodissociation region as a function of visual extinction A_V . Reprinted from Wolfire et al. (2022).

1 Introduction

The interstellar medium (ISM) is composed of gas and dust between stars in galaxies. The ISM is site of star formation and takes up around $\sim 10\%$ of total baryonic mass [cite Drain2011](#). In return, the radiation field produced by stars is responsible for the heating the gas and dust that cool in bright line and continuum emission. These emission lines provide information about the physical conditions inside the ISM, such as the temperature, density and chemical composition.

Models have long been developed to help us interpret these

The 1D slab geometry may not be appropriate in some cases, and the curvature of the cloud surface needs to be taken into account in order to reproduce the line profiles. A common technique is to use a time-dependent hydrodynamic simulation to obtain the density and velocity fields and then to postprocess it with a PDR code to obtain the steady-state chemical abundances and thermal equilibrium gas temperature (e.g., Levrier et al. 2012).

1.1 Photodissociation Regions (PDRs)

Photodissociation regions (PDRs) are regions where far-ultraviolet (FUV; $6 \text{ eV} < h\nu < 13.6 \text{ eV}$) radiation dominates the chemistry or heating processes (Tielens and Hollenbach 1985). PDRs span a wide range of incident FUV fluxes and densities, including all neutral gas in the interstellar medium (ISM) and molecular layers where FUV radiation drives molecule formation.

1.2 The Horsehead Nebula

In order to compare with observations, we need to convert the distance unit cm used the in MeudonPDR code into the arcsec unit used in observation,

$$\alpha['] = \frac{d[\text{pc}]}{400 \text{ pc}} \frac{1 \text{ arcsec}}{1 \text{ rad}} \quad (1)$$

where 400 pc (Menten et al. 2007; Schlafly et al. 2014) is the distance to the horsehead nebula.



Figure 2: [Horsehead Nebula captured by the Hubble Space Telescope \(HST\) in 2013](#). The image was created from Hubble data from proposal [12812](#). Illustration Credit: [NASA](#), [ESA](#), and Z. Levay ([STScI](#))

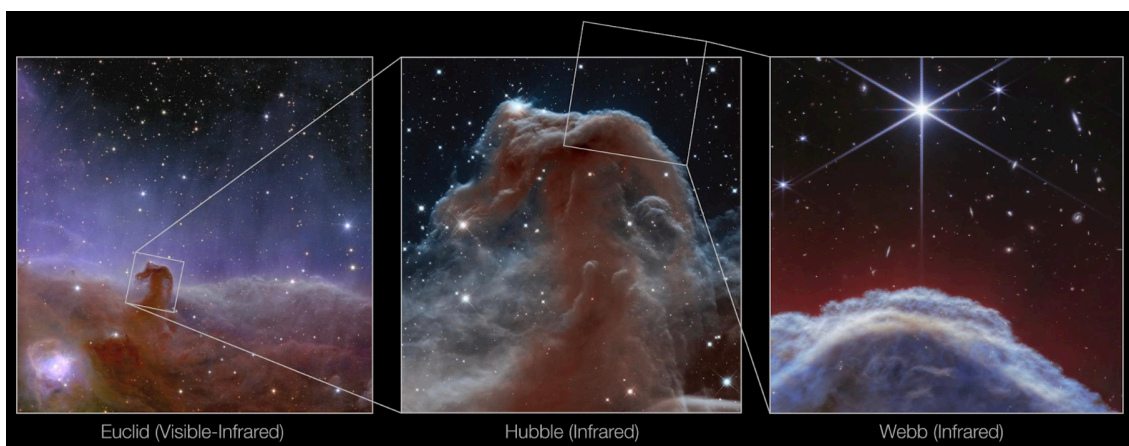


Figure 3: [Three views of the Horsehead Nebula](#). The first image (left) features the Horsehead Nebula as seen by ESA's Euclid telescope. The second image (middle) shows the NASA/ESA Hubble Space Telescope's infrared view of the Horsehead Nebula. The third image (right) features a new view of the Horsehead Nebula from the NASA/ESA/CSA James Webb Space Telescope's NIRCam (Near-InfraRed Camera) instrument.

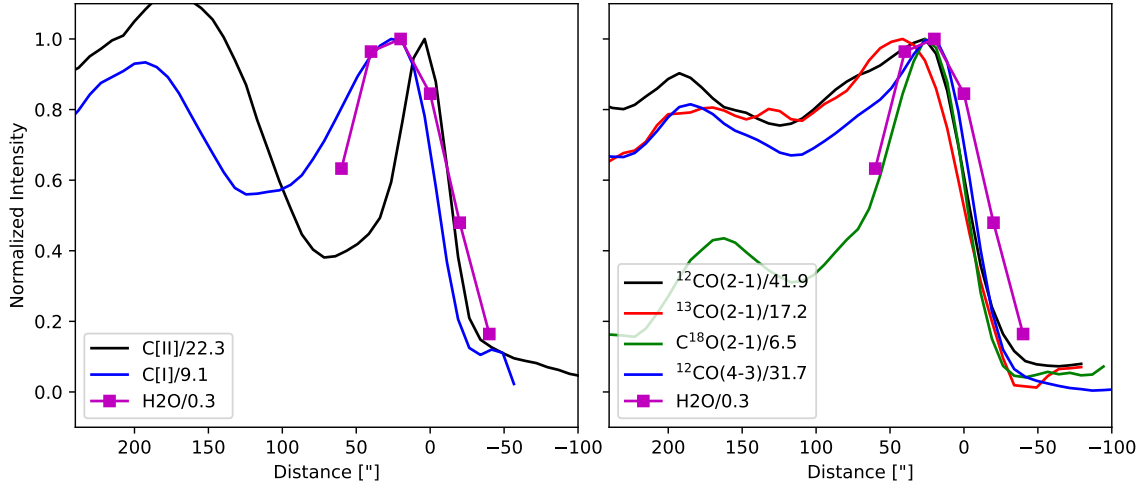


Figure 4: Observed line profiles of the Horsehead Nebula by Herschel HIFI. Reproduced from [cite the original paper](#). The ^{13}CO lines has been removed due to bad weather condition during the observation.

2 Data

The observational data used in this study (Fig. 4) were obtained from the Heterodyne Instrument for the Far-Infrared (HIFI) (de Graauw et al. 2010) onboard the Herschel Space Observatory (Pilbratt et al. 2010). All data are convolved to the spatial resolution of the HIFI H₂O data, 38.1 arcsec. The observed molecular species were detected at specific wavelengths corresponding to transitions listed in Table 1.

Notation	Species	Upper Level	Lower Level	Frequency (GHz)
H ₂ O	H ₂ O	J=1, Ka=1, Kc=0	J=1, Ka=0, Kc=1	557.30
C[II]	C ⁺	2P J=3/2	2P J=1/2	1902.59
C[I]	C	3P J=1	3P J=0	492.02
^{12}CO (2-1)	CO	v=0, J=2	v=0, J=1	230.538
^{12}CO (4-3)	CO	v=0, J=4	v=0, J=3	461.041
^{13}CO (2-1)	^{13}CO	v=0, J=2	v=0, J=1	220.399
C ^{18}O (2-1)	C ^{18}O	v=0, J=2	v=0, J=1	219.560

Table 1: Parameters of transitions in the observation data used in this study.

3 Methods

3.1 The MeudonPDR code

A significant heterogeneity exists among the available PDR models, which differ in their geometry, physical and chemical structures, and model parameters. Röllig et al. (2007) suggest that the choice of a specific code should depend on the physical and chemical processes implemented in the code, as well as the characteristics of the emission source.

In this project, I used the MeudonPDR code (Bron 2014; Bron et al. 2014, 2016; Goicoechea and Le Boulrot 2007; Gonzalez Garcia et al. 2008; Le Boulrot et al. 2012;

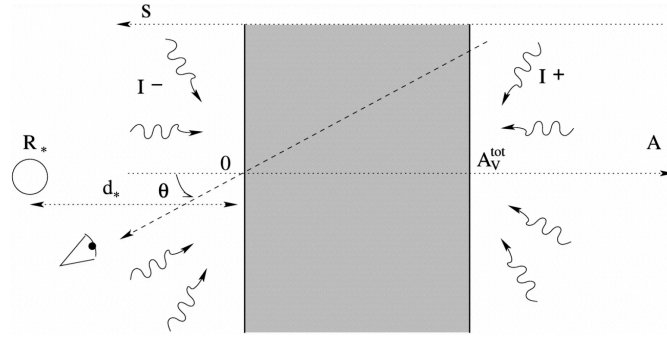


Figure 5: Scheme of the slab geometry of the MeudonPDR code. Reprinted from Le Petit et al. (2006).

Le Petit et al. (2006) to simulate the Horsehead Nebula. The MeudonPDR code models a stationary one-dimensional (1D), plane-parallel slab of gas and dust illuminated by an ultraviolet (UV) radiation field from one or both sides (Fig. 5). At each iteration, the code solves the UV radiative transfer in both the continuum and lines, followed by the chemical balance, and finally the level populations and thermal balance. The code outputs the level populations, the gas temperature, and the chemical abundances as a function of the depth into the cloud, with optional output of the radiation field. The physical parameters used to model the Horsehead PDR are summarized in Table 2.

Cloud size (A_V^1)	40
Proton density ² (n_H)	$3 \times 10^4 - 3 \times 10^6 \text{ cm}^{-3}$
Pressure ² (P)	$1 \times 10^6 - 1 \times 10^7 \text{ K cm}^{-3}$
ISRF	shape: Mathis ³ , geometry: beam_isot ⁴
ISRF scaling factor	$G_0^{\text{obs}} = 100$, $G_0^{\text{back}} = 0.04^5$
UV radiative transfer method	FGK approximation, or exact H_2 self- and mutual shielding ⁶
Turbulent velocity dispersion	2 km s^{-1} ⁷
Extinction Curve	HD38087 ⁸
$R_V = A_V/E(B - V)$	5.50
$C_D = N_H/E(B - V)$	1.57×10^{22}

Table 2: Key physical parameters used to model the Horsehead PDR in the MeudonPDR code.¹Visual extinction, $A_V \equiv 2.5 \log_{10}(I_V^0/I_V^{\text{obs}})$. ²Proton density is used in constant density models, and pressure is used in constant pressure models(see Section 3.1.1). ³Mathis et al. (1983). ⁴Perpendicular on observer side, isotropic on back side. ⁵In Habing units, as defined in Le Petit et al. (2006). ⁶ See Section. 3.1.2. ⁷Only used in Doppler line broadening. ⁸Fitzpatrick and Massa (1990). Other parameters use default values. More descriptions can be found in the [MeudonPDR code documentation](#).

3.1.1 Constant Pressure vs. Constant Density

The density structure of a PDR model, whether it assumes constant density, constant pressure, or a user-defined density profile, can significantly influence the simulation results (Wolfire et al. 2022). As shown in Fig. 6 and Fig. 7, I compare the cloud structure computed with constant pressure and constant density assumptions, illustrating the differences in the resulting PDR structures. The values $n_H = 3 \times 10^5 \text{ cm}^{-3}$ for the constant

density model and $P = 5 \times 10^6 \text{ K cm}^{-3}$ for the constant pressure model are based on Maillard (2023). In the constant pressure model, the transition from atomic to molecular hydrogen occurs at higher visual extinction (Fig. 6), and the total physical thickness of the cloud is larger (Fig. 7). The temperature profile in the constant pressure model is also more gradual. Additional comparisons between various constant density models and constant pressure models are provided in the appendix.

Observations of the Horsehead Nebula reveal a steep density gradient in the PDRs (Guzmán et al. 2011; Habart et al. 2005). Hernández-Vera et al. (2023) showed that constant density models fail to reproduce the observed structures, and neither do previously proposed density profile prescriptions. Furthermore, recent observations from ALMA and Herschel indicate that the warm layer of PDRs is indeed isobaric, with by relatively high thermal pressures (Bron et al. 2018; Goicoechea et al. 2016; Joblin et al. 2018; Maillard et al. 2021; Marconi et al. 1998; Wu et al. 2018). Based on these findings, I adopt a constant pressure model with $P = 5 \times 10^6 \text{ K cm}^{-3}$ for the subsequent analysis.

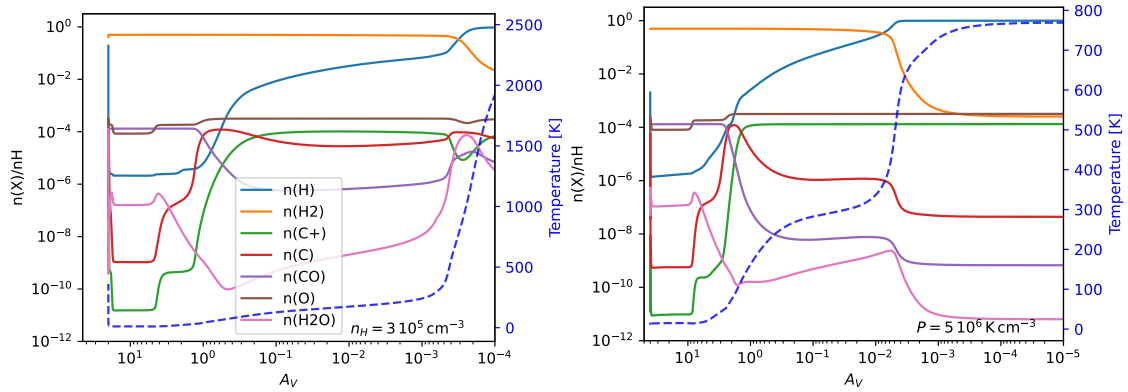


Figure 6: Comparison of the cloud structure computed with constant density $n_H = 3 \times 10^5 \text{ cm}^{-3}$ (left) and constant pressure $P = 5 \times 10^6 \text{ K cm}^{-3}$ (right), with a shared legend displayed in the left plot. All other parameters are the same as those listed in Table. 2.

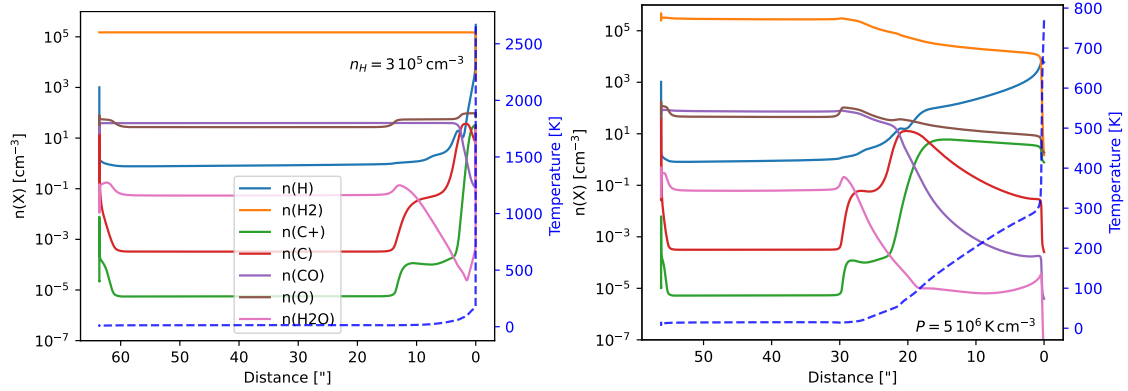


Figure 7: Similar to Fig. 6, but using physical units, with arcseconds as the distance unit and the densities represented by their actual values (not normalized by proton density).

3.1.2 Models with Exact Radiative Transfer of H_2

There are two options available in the MeudonPDR code for treating radiative transfer in the UV. The first is the FGK approximation (Federman et al. 1979), which accounts for the self-shielding of H and H_2 molecules. Self-shielding occurs when molecules absorb

radiation in their own spectral lines, reducing the flux available to penetrate deeper into the cloud. However, the FGK approximation neglects mutual shielding, where the overlap and interaction of absorption lines between different species or multiple lines of the same species further attenuate the radiation field.

The second, more accurate approach, is to compute the radiative transfer exactly (Goicoechea and Le Bourlot 2007; Gonzalez Garcia et al. 2008). This method explicitly includes mutual shielding for a limited number of energy levels of H and H₂. For higher energy levels, the FGK approximation is still applied, as their contribution is expected to be negligible due to their low population. Although the exact method is computationally more intensive, it allows a more accurate treatment of the UV radiation field, which, in turn, affects the PDR structure. For instance, with the exact method, the increased attenuation of the radiation field shifts the H/H₂ transition layer to lower extinction depths (Goicoechea and Le Bourlot 2007).

add a plot of the radiation field to show the effect of radiative shielding
figures comparing with and without h2 rt

3.1.3 Models with Surface Chemistry

In the ISM, direct gas-phase formation of molecules is very inefficient. Instead, molecules are formed on the surfaces of dust grains, which act as catalysts by providing a surface for adsorbed atoms to meet and react. The grains also absorb the excess energy released by the formation process, preventing dissociation that would otherwise occur in the gas-phase formation. The formation of H₂ is a key demonstration of the importance of this process, as the gas-phase formation rate of H₂ is much lower than the rate required to explain the observed abundance of H₂ in the ISM (Gould and Salpeter 1963; Hollenbach and Salpeter 1971). In addition to chemical reactions, dust grains also play a role in the sublimation and freeze-out of molecules, leading to “jumps” or “drops” in molecular profiles at specific temperatures (Herbst and van Dishoeck 2009).

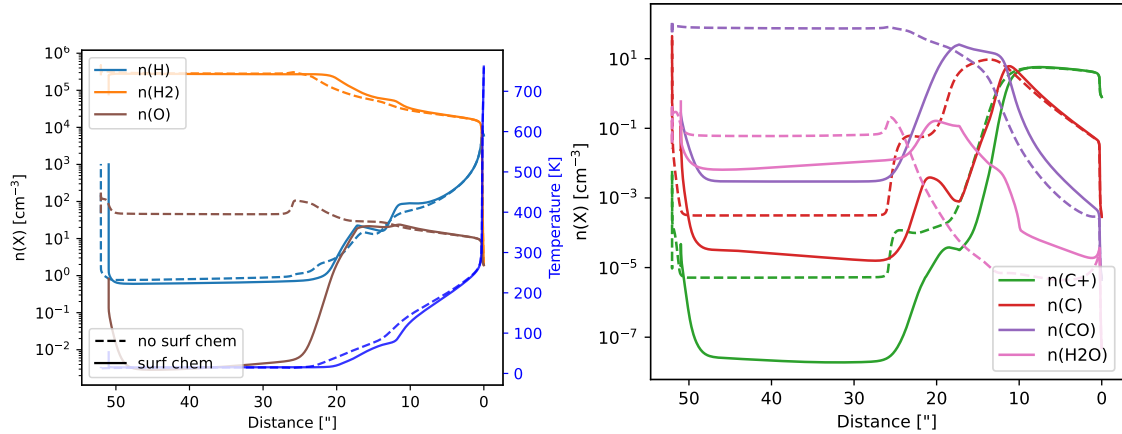


Figure 8: Comparison of abundances for models computed with and without surface chemistry: H species and O (left), and C species, CO, and H₂O (right).

In Fig. 8, I compare the PDR models computed with and without surface chemistry. The inclusion of surface reactions leads to an earlier rise in the abundances of $n(\text{H}_2)$, $n(\text{CO})$ and $n(\text{H}_2\text{O})$ due to enhanced production on dust grain surfaces. At greater depths within the cloud, the abundances of almost all molecules decrease in the model with surface chemistry because of the freeze-out of molecules onto the dust grains. Grains also reduce the gas temperature, as they absorb the energy released during molecule forma-

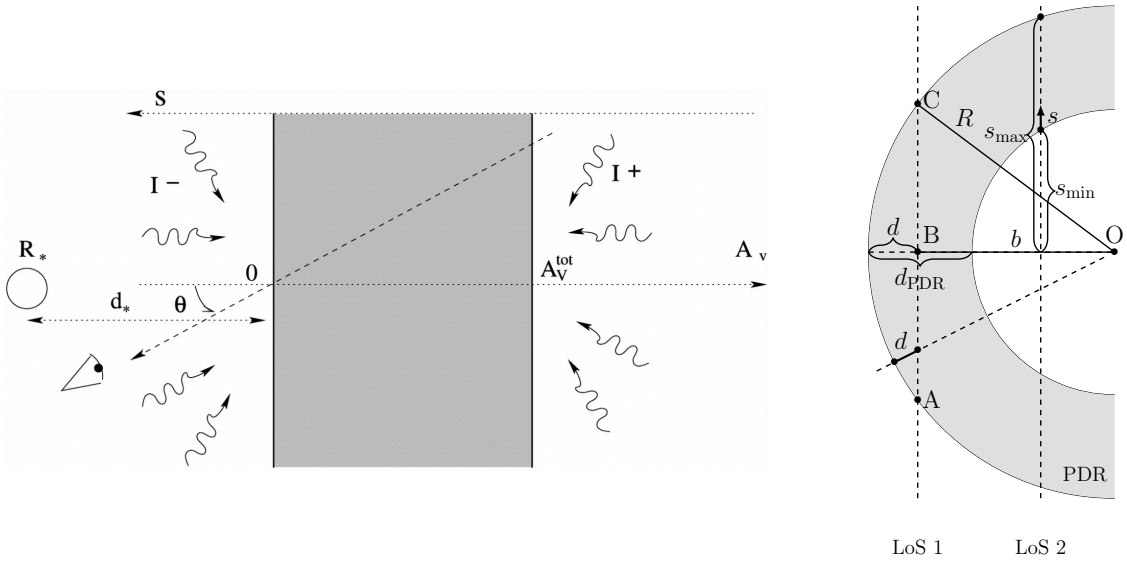


Figure 9: Left: scheme of the slab geometry of the MeudonPDR code. Reprinted from Le Petit et al. (2006) Right: scheme of the plane-parallel geometry of the PDR wrapper.

tion, as shown in the left panel. Therefore, including surface chemistry in PDR models is crucial for accurately describing the molecular abundances and the gas temperature.

To summarize the model comparisons in this section, we will use the constant pressure model with exact radiative transfer of H_2 and surface chemistry to consider the curvature of the cloud surface in the following sections.

3.2 Geometry

In order to model the curvature of the cloud surface, we approximate the surface using plane-parallel geometry, as shown in Fig. 9.

More precisely, we consider the PDR region as the outermost shell embedded in a fictitious spherical cloud, whose radius R will need to be determined by the user and is given as a parameter to the wrapper code.

A line of sight will be defined by an impact parameter b , which is the distance from the line-of-sight (LoS) to the center of the cloud.

From the output of the MeudonPDR code, we have the number densities of levels as a function of the depth into the cloud, so we need to know the depth (i.e., the distance to the cloud surface) corresponding to each point along the LoS, we denote this quantity as d .

Using Pythagorean theorem, we can easily establish that

$$d = R - \sqrt{s^2 + b^2} \quad (2)$$

3.3 Column Density

The wrapper code take as input:

- the level number densities computed by the MeudonPDR code, as a function of the depth into the cloud, $n_X(d)$;
- the radius of the fictitious spherical cloud, R ;
- the impact parameter of the LoS, b .

The algorithm goes as follow

1. interpolate the level number density to enable the computation of the density at any valid given value of depth, $n_X(d) = f(d)$;
2. compute the range of distances inside the PDR region along the LoS

$$s_{\max} = \sqrt{R^2 - b^2}, s_{\min} = \begin{cases} 0 & b > R - d_{\text{PDR}} \\ \sqrt{(R - d_{\text{PDR}})^2 - b^2} & b < R - d_{\text{PDR}} \end{cases} \quad (3)$$

3. convert the distance along the LoS to depth from the surface of the cloud, and compute the level number density

$$n_X(s) = f(R - \sqrt{s^2 + b^2}); \quad (4)$$

4. the column density for a given LoS with impact parameter b is given by

$$N_X(b) = 2 \int_{s_{\min}}^{s_{\max}} n_X(s') ds'. \quad (5)$$

3.4 Radiative transfer equation

In the previous calculation of the column densities, we have made the assumption that all lines are optically thin; in fact, some of the lines can be optically thick, which explains the difference in the shape of the curve in observations for different lines in Fig 4.

To account for line extinction inside the cloud, we need to solve the radiative transfer equation along the LoS [cite see, for example, Eq \(1.67\) Rybicki?](#):

$$\frac{dI_\nu}{ds} = A_{ul}n_u \frac{h\nu}{4\pi} \phi(\nu) + B_{ul}n_u \frac{h\nu}{4\pi} I_\nu \phi(\nu) - B_{lu}n_l \frac{h\nu}{4\pi} I_\nu \phi(\nu), \quad (6)$$

where n_u and n_l are the number densities of the upper and lower levels of the transition, respectively, h is the Planck's constant, ν is the frequency of the transition, and $\phi(\nu)$ is the line profile. We assume that the emission and absorption profiles are the same and we neglect scattering [justify?](#). A_{ul}, B_{ul}, B_{lu} are the Einstein coefficients for this transition, which are related by the Einstein relation [references](#)

$$B_{ul} = \frac{c^2}{2h\nu_{ul}^3} A_{ul}, \quad g_l B_{lu} = g_u B_{ul}, \quad (7)$$

where g_u and g_l are the degeneracies of the upper and lower levels, respectively.

For consistency, we keep the same values for the Einstein coefficients as in the MeudonPDR code, which are taken from [references?](#).

In the PDR, turbulences are the dominant line broadening process [references?](#) [a bit more on line broadening in the intro?](#), in which case the line profile $\phi(\nu)$ is a Gaussian profile in the form [references](#)

$$\phi(\nu) = \frac{1}{\sigma_\nu \sqrt{2\pi}} \exp\left(-\frac{(\nu - \nu_0)^2}{2\sigma_\nu^2}\right), \quad (8)$$

where

$$\sigma_\nu = \frac{\sqrt{2}}{2} \Delta\nu_D, \quad \Delta\nu_D = \frac{\nu_0}{c} \sqrt{\frac{2kT}{m} + v_{\text{turb}}^2}. \quad (9)$$

The turbulent velocity v_{turb} is a parameter in the MeudonPDR code, with a default value of 2 km s^{-1} . T is the temperature, and m is the mass of the line-emitting species. For the mass we use the same value as the MeudonPDR code (as defined in , taken from [Scientific Instrument Services \(SIS\) database?](#) [change name?](#)

The line profile is normalized so that $\int_0^\infty \phi(\nu) d\nu = 1$. In practice, we truncate the line profile at 5σ [add a figure to demonstrate that this is reasonable for the lines concerned?](#), i.e., the normalization becomes

$$\int_{\nu_0-5\sigma}^{\nu_0+5\sigma} \phi(\nu) d\nu = 1 \quad (10)$$

To solve the radiative transfer equation, we also need a background intensity I_0 . For this we use the isotropic specific intensity on the observation side output by the MeudonPDR code, in the `_IncRadField.dat` file. [add explanation that our implementation is only valid for isotropic radiation and explains why we couldn't implement a more generic background specific intensity.](#)

The external radiation field in the `_IncRadField.dat` file is in units of $\text{erg cm}^{-2} \text{ s}^{-1} \text{ sr}^{-1} \text{ \AA}^{-1}$, so we need to convert the specific intensity in to $\text{erg cm}^{-2} \text{ s}^{-1} \text{ sr}^{-1} \text{ Hz}^{-1}$,

$$I_\nu |d\nu| = I_\lambda |d\lambda| \Rightarrow I_\nu = I_\lambda \left| \frac{d\lambda}{d\nu} \right| = I_\lambda \frac{c}{\nu^2} = I_\lambda \frac{\lambda^2}{c} \quad (11)$$

$$\lambda = \frac{c}{\nu} \Rightarrow d\lambda = -\frac{c}{\nu^2} d\nu \Rightarrow \left| \frac{d\lambda}{d\nu} \right| = \frac{c}{\nu^2} = \frac{\lambda^2}{c} \quad (12)$$

It is often more convenient to do a change of variable and integrate over optical depth

$$\frac{dI_\nu}{d\tau_\nu} = S_\nu - I_\nu, \quad (13)$$

with

$$\tau_\nu = \alpha_\nu ds, \quad S_\nu = \frac{j_\nu}{\alpha_\nu} \quad (14)$$

$$\alpha_\nu = \frac{h\nu}{4\pi} \phi(\nu) (B_{lu}n_l - B_{ul}n_u) \quad (15)$$

$$j_\nu = A_{ul}n_u \frac{h\nu}{4\pi} \phi(\nu) \quad (16)$$

To test the solver, we first solve the radiative transfer with constant density profiles of both the lower and upper level, then the radiative transfer equation becomes

$$\frac{dI_\nu}{ds} = c_1 + c_2 I_\nu, \quad (17)$$

with

$$c_1 = A_{ul}n_u \frac{h\nu}{4\pi} \phi(\nu) = \text{cst}$$

$$c_2 = (B_{ul}n_u - B_{lu}n_l) \frac{h\nu}{4\pi} \phi(\nu) = \text{cst}.c$$

The analytical solution is

$$I_\nu(s) = \left(I_0 + \frac{c_1}{c_2} \right) e^{c_2 s} - \frac{c_1}{c_2}. \quad (18)$$

For example, if we consider the CO transition from $v=0, J=2$ to $v=0, J=1$, with a constant density profile of $n_u = 2 \text{ cm}^{-3}$, $n_l = 2 \text{ cm}^{-3}$, $A_{ul} = 6.911 \times 10^{-7} \text{ s}^{-1}$

- $h\nu/4\pi = 4.86234284e - 16$
- $A_{ul} = 6.911e - 07$
- $B_{ul} = 3825410.21021763$
-

3.5 Convolution

4 Results and Discussion

4.1 Cloud Surface Curvature

4.2 Line Profiles

5 Conclusions

References

- Bron, E. (2014). “Stochastic processes in the interstellar medium”. 2014PA077169. PhD thesis, 1 vol. (382 p.)
- Bron, E., Le Bourlot, J., and Le Petit, F. (2014). “Surface chemistry in the interstellar medium. II. H_2 formation on dust with random temperature fluctuations”. In: A&A 569, A100, A100. DOI: [10.1051/0004-6361/201322101](https://doi.org/10.1051/0004-6361/201322101).
- Bron, E., Le Petit, F., and Le Bourlot, J. (2016). “Efficient ortho-para conversion of H_2 on interstellar grain surfaces”. In: A&A 588, A27, A27. DOI: [10.1051/0004-6361/201527879](https://doi.org/10.1051/0004-6361/201527879).
- Bron, E. et al. (2018). “Photoevaporating PDR models with the Hydra PDR Code”. In: *arXiv e-prints*, arXiv:1801.01547, arXiv:1801.01547. DOI: [10.48550/arXiv.1801.01547](https://doi.org/10.48550/arXiv.1801.01547).
- de Graauw, T. et al. (2010). “The Herschel-Heterodyne Instrument for the Far-Infrared (HIFI)”. In: A&A 518, L6, p. L6. DOI: [10.1051/0004-6361/201014698](https://doi.org/10.1051/0004-6361/201014698).
- Federman, S. R., Glassgold, A. E., and Kwan, J. (1979). “Atomic to molecular hydrogen transition in interstellar clouds.” In: ApJ 227, pp. 466–473. DOI: [10.1086/156753](https://doi.org/10.1086/156753).
- Fitzpatrick, E. L. and Massa, D. (1990). “An Analysis of the Shapes of Ultraviolet Extinction Curves. III. an Atlas of Ultraviolet Extinction Curves”. In: ApJS 72, p. 163. DOI: [10.1086/191413](https://doi.org/10.1086/191413).
- Goicoechea, J. R. and Le Bourlot, J. (2007). “The penetration of Far-UV radiation into molecular clouds”. In: A&A 467.1, pp. 1–14. DOI: [10.1051/0004-6361:20066119](https://doi.org/10.1051/0004-6361:20066119).
- Goicoechea, J. R. et al. (2016). “Compression and ablation of the photo-irradiated molecular cloud the Orion Bar”. In: Nature 537.7619, pp. 207–209. DOI: [10.1038/nature18957](https://doi.org/10.1038/nature18957).
- Gonzalez Garcia, M. et al. (2008). “Radiative transfer revisited for emission lines in photon dominated regions”. In: A&A 485.1, pp. 127–136. DOI: [10.1051/0004-6361:200809440](https://doi.org/10.1051/0004-6361:200809440).
- Gould, R. J. and Salpeter, E. E. (1963). “The Interstellar Abundance of the Hydrogen Molecule. I. Basic Processes.” In: ApJ 138, p. 393. DOI: [10.1086/147654](https://doi.org/10.1086/147654).
- Guzmán, V. et al. (2011). “ H_2CO in the Horsehead PDR: photo-desorption of dust grain ice mantles”. In: A&A 534, A49, A49. DOI: [10.1051/0004-6361/201117257](https://doi.org/10.1051/0004-6361/201117257).
- Habart, E. et al. (2005). “Density structure of the Horsehead nebula photo-dissociation region”. In: A&A 437.1, pp. 177–188. DOI: [10.1051/0004-6361:20041546](https://doi.org/10.1051/0004-6361:20041546).
- Herbst, E. and van Dishoeck, E. F. (2009). “Complex Organic Interstellar Molecules”. In: ARA&A 47.1, pp. 427–480. DOI: [10.1146/annurev-astro-082708-101654](https://doi.org/10.1146/annurev-astro-082708-101654).
- Hernández-Vera, C. et al. (2023). “The extremely sharp transition between molecular and ionized gas in the Horsehead nebula”. In: A&A 677, A152. DOI: [10.1051/0004-6361/202347206](https://doi.org/10.1051/0004-6361/202347206).
- Hollenbach, D. and Salpeter, E. E. (1971). “Surface Recombination of Hydrogen Molecules”. In: ApJ 163, p. 155. DOI: [10.1086/150754](https://doi.org/10.1086/150754).
- Joblin, C. et al. (2018). “Structure of photodissociation fronts in star-forming regions revealed by Herschel observations of high-J CO emission lines”. In: A&A 615, A129, A129. DOI: [10.1051/0004-6361/201832611](https://doi.org/10.1051/0004-6361/201832611).
- Le Bourlot, J. et al. (2012). “Surface chemistry in the interstellar medium. I. H_2 formation by Langmuir-Hinshelwood and Eley-Rideal mechanisms”. In: A&A 541, A76, A76. DOI: [10.1051/0004-6361/201118126](https://doi.org/10.1051/0004-6361/201118126).
- Le Petit, F. et al. (2006). “A Model for Atomic and Molecular Interstellar Gas: The Meudon PDR Code”. In: ApJS 164.2, pp. 506–529. DOI: [10.1086/503252](https://doi.org/10.1086/503252).
- Maillard, V. (2023). “Model of photo-evaporating fronts in star forming regions”. Theses. Université Paris sciences et lettres.

- Maillard, V., Bron, E., and Le Petit, F. (2021). “Dynamical effects of the radiative stellar feedback on the H I-to-H₂ transition”. In: A&A 656, A65, A65. DOI: [10.1051/0004-6361/202140865](https://doi.org/10.1051/0004-6361/202140865).
- Marconi, A. et al. (1998). “Near infrared spectra of the Orion bar”. In: A&A 330, pp. 696–710. DOI: [10.48550/arXiv.astro-ph/9710051](https://doi.org/10.48550/arXiv.astro-ph/9710051).
- Mathis, J. S., Mezger, P. G., and Panagia, N. (1983). “Interstellar radiation field and dust temperatures in the diffuse interstellar medium and in giant molecular clouds”. In: A&A 128, pp. 212–229.
- Menten, K. M. et al. (2007). “The distance to the Orion Nebula”. In: A&A 474.2, pp. 515–520. DOI: [10.1051/0004-6361:20078247](https://doi.org/10.1051/0004-6361:20078247).
- Pilbratt, G. L. et al. (2010). “Herschel Space Observatory. An ESA facility for far-infrared and submillimetre astronomy”. In: A&A 518, L1, p. L1. DOI: [10.1051/0004-6361/201014759](https://doi.org/10.1051/0004-6361/201014759).
- Röllig, M. et al. (2007). “A photon dominated region code comparison study”. In: A&A 467.1, pp. 187–206. DOI: [10.1051/0004-6361:20065918](https://doi.org/10.1051/0004-6361:20065918).
- Schlafly, E. F. et al. (2014). “A Large Catalog of Accurate Distances to Molecular Clouds from PS1 Photometry”. In: ApJ 786.1, 29, p. 29. DOI: [10.1088/0004-637X/786/1/29](https://doi.org/10.1088/0004-637X/786/1/29).
- Tielens, A. G. G. M. and Hollenbach, D. (1985). “Photodissociation regions. I. Basic model.” In: ApJ 291, pp. 722–746. DOI: [10.1086/163111](https://doi.org/10.1086/163111).
- Wolfire, M. G., Vallini, L., and Chevance, M. (2022). “Photodissociation and X-Ray-Dominated Regions”. In: *Annual Review of Astronomy and Astrophysics* 60. Volume 60, 2022, pp. 247–318. DOI: <https://doi.org/10.1146/annurev-astro-052920-010254>.
- Wu, R. et al. (2018). “Constraining physical conditions for the PDR of Trumpler 14 in the Carina Nebula”. In: A&A 618, A53, A53. DOI: [10.1051/0004-6361/201832595](https://doi.org/10.1051/0004-6361/201832595).